Supporting Information

Grigoryev et al. 10.1073/pnas.0903280106

SI Text

Refinements to the Mesoscale Model. Atomic resolution computational approaches such as molecular dynamics simulations cannot capture the dynamics and equilibrium properties of large, flexible and complex biopolymers such as the chromatin fiber. Over a period of 6 years, we have developed a mesoscopic model of chromatin (1–8) that dramatically reduces the total degrees of freedom of the system, thus alleviating the prohibitive computational demands of atomistic simulations, whereas incorporating key features of the chromatin fiber. Essentially, the nucleosome surface is represented as a charged body with point charges distributed to approximate the atomistic Poisson-Boltzmann electric field; the linker DNA is represented using beads modeled by the wormlike chain model of DNA (see Fig. 1 in reference 8), i.e., this model accounts for nonuniform distribution of charges. Such a model captures the essential physics of chromatin such as its electrostatics, mechanics, conformational flexibility, and structural irregularity because of thermal fluctuations, whereas averaging over less important effects arising from protein/DNA sequence, hydrogen-bonding, and atomistic fluctuations. The model makes chromatin fibers as large as 48-nucleosomes long amenable to long-time, large-scale simulations by Brownian dynamics and Monte Carlo methods.

The model of chromatin developed recently (6, 7) also accounts explicitly for histone tail flexibility; however, it only treats monovalent salt and does not account for the effects of linker histones on chromatin architecture. Additionally, this model is based on a 1.75-turn wrapping of DNA in the nucleosome according to the 1997 crystal structure of the nucleosome (9) invoking crossed nucleosome linkers; a recent crystal structure (10) suggests a reduced wrapping of 1.7 turns and multiple cryoelectron microscopy (11, 12), AFM (13, 14), and FRET (15) studies reveal noncrossed linkers in nucleosome core arrays.

The refined mesoscale model of chromatin used in the present study improves upon the prior model through the inclusion of both linker histones and the effects of magnesium ions, as well as better handling of the nucleosomes linker DNA geometry. The remaining components in the refined model, i.e., the nucleosome core, linker DNA, and histone tails, are treated as in the prior model (5, 6). Below we discuss these refined components of the mesoscale model developed in this study—linker histone modeling, treatment of magnesium, and modified linker DNA-nucleosome geometry—and the tailored Monte Carlo methodology adopted for generating an ensemble of oligonucleosome configurations. Details of the complete refined model as well the various tests we have conducted to validate this model are provided in our most recent publication (8).

Linker histone modeling. The linker histone is modeled based on the structure of rat H1d linker histone predicted via fold recognition and molecular modeling (16, 17). H1d consists of an N-terminal region of 33 residues, globular-shaped central region of 76 residues, and highly charged C termini of 110 residues. In our model, we represent the globular domain by a single charged bead and the C-terminal domain by 2 charged beads. The 3-linker histone beads are placed on the dyad axis of each nucleosome at distances r = 6.2, 8.8, and 11.4 nm from the nucleosome center (Fig. 1 in reference 8) as suggested (16, 18). We assume that the linker histones remain rigidly attached to their parent nucleosomes.

Each bead is assigned an optimized charge at its center so that the resulting Debye-Hückel electrostatic potential of the coarse-grained model reproduces the electrostatic potential of the atomistic linker histone obtained by solving the complete nonlinear Poisson-Boltzmann equation as done for the nucleosome core (2, 3). Specifically, this yields charges of $+12.4e$ for the globular bead and $+29.9e$ for each of the 2 C-terminal beads at 0.15 M salt and $+4.6e$ and $+6.4e$ at 0.01 M salt. In addition, each bead is assigned an excluded volume via a Lennard-Jones potential with an energy parameter k_{eV} = 0.001 kcal/mol and size parameters of σ_g = 3.6 nm and 3.2 nm for the globular and C termini beads, respectively. We neglect the short, relatively uncharged, N-terminal region. The linker histone beads interact with all chromatin components except their parent nucleosomes through excluded volume (Lennard-Jones potential) and electrostatic interactions (Debye-Hückel potential). Note that this model does not account for binding and dissociation of the linker histones from the favored nucleosome dyad position.

Magnesium modeling. The analytical estimate of the electrostatic screening length of 150 mM NaCl and 1 mM $MgCl_2$ using the Debye-Hückel theory (κ = 1.52 nm^{-1}), is only nominally larger than that obtained for 150 mM monovalent salt alone (1.48 nm^{-1}) and is not sufficient to account for the extensive chromatin compaction obtained with the addition of Mg^{2+} ions. This has also been verified through simulations of our mesoscale model where κ has been artificially set to the slightly larger value (1.52 nm^{-1}). Additionally, our coarse-grained model of linker DNA cannot automatically capture the increase in DNA flexibility (decrease in persistence length) at 1 mM divalent cations (19, 20).

This has prompted us to take a phenomenological approach toward modeling the effect of 1 mM Mg^{2+}. Basically, to model the effect of Mg^{2+}, we further reduce the repulsion among linker DNA by setting a Debye length of κ = 2.5 nm^{-1} based on the argument that, at the fully condensed state of chromatin, the linker DNAs are almost touching one another. Thus, setting κ to the inverse of the diameter of DNA (~2.5 nm) allows linker DNA to come as close as their diameters. Additionally, we change the persistence length of the linker DNAs to 30 nm (from 50 nm with monovalent salt) according to published data (19, 20). With this phenomenological model, we expect to capture the essence of Mg^{2+} ion induced chromatin compaction. A more specialized modeling of Mg^{2+} effects is not compatible with the mesoscale chromatin model and would be far more computationally intensive.

Refinement of DNA-wrapping angle. Our earlier oligonucleosome models (1–7) were based on 1.75 turn of the nucleosome-wound DNA (i.e., θ_o was set to 90 °; see discussion on nucleosome/linker DNA mechanics in *SI Text*). The model yielded the correct salt-dependent folding/unfolding of oligonucleosomes (in terms of the sedimentation coefficients), salt-dependent contraction/extension of histone tails, diffusion coefficients of short oligonucleosomes, and internucleosomal interaction energies. However, the model did not reproduce the internucleosomal interaction pattern obtained experimentally, i.e., the model predicted dominant interactions between nucleosome i and nucleosomes i ± 3 and i ± 4, whereas the EMANIC experiments of the current study indicate dominant interactions between nucleosomes i and i ± 2. In addition, the model does not yield the correct mixture of open and crossed linker DNA conformations seen experimentally.

To this end, we have improved this model based on more recent crystal data suggests a reduced wrapping of 1.7 turns of wound DNA (9) that corresponds to a value of θ_o = 108° for the linker DNA entry/exit trajectory orientation (8). These param-

eters produce a mixture of crossed and uncrossed linker DNA geometries at high monovalent salt (20% open and 80% crossed) and an internucleosomal interaction pattern dominated by (i ± 2) interactions, in agreement with the experimental findings (15) and this work, respectively. We found that this parameter change did not affect other properties like sedimentation coefficients and internucleosomal interaction energies, as reported previously (5, 6).

Monte Carlo sampling methodology. We use the Monte Carlo methodology developed earlier by us that combines 3 local and 1 global "move" to efficiently sample the ensemble of oligonucleosome conformations under constant temperature conditions (6, 7). The local moves include translation, rotation, and tail regrowth move and the global move includes pivot moves. A fifth move called "end-transfer configurational bias MC" method developed recently by our group (7) is not used for the present study and is therefore not described. The rotation, translation, regrowth, and pivot Monte Carlo moves are attempted with frequencies of 0.1:0.1:0.6:0.2, respectively. Each simulation run consists of 20–40 million Monte Carlo steps, and ≈100,000 configurations were used for the averaging procedure. A constant temperature of 293 K and monovalent salt concentrations of 0.01 and 0.15 M are used. All results are averages >100,000 configurations (24-unit oligonucleosomes) collected from 12 Monte Carlo runs: Different initial pseudorandom number seeds used for 4 different initial configurations, and each of these 4 run at 3 different intrinsic twist values (0 ° ± 12 °) to account for small variations of the DNA twist from 1 nucleosome to the next. Note that for the 7-segment/6-bead linker DNA length used, the 21-nm linker DNA corresponds to 61.8 bp or 6 full turns using the crystallographic average twist of 10.3 bp/turn for chromatin fibers (21).

Monte Carlo simulations of +LH+Mg chromatin started from the 4 different oligonucleosome configurations (zigzag with parallel and perpendicular nucleosomes, and solenoid with parallel and perpendicular nucleosomes), as described in elsewhere (5, 6) do not converge to a single global equilibrium (stable) structure, but rather converge upon to 2 basic locally stable structures (Fig. S3). Structures in *A* and *B* lead to predominantly straight linker DNA configurations, whereas *C* and *D* lead a large population of bent linker DNA states. However, there are significant departures in the patterns from their starting configurations, suggesting the effectiveness of the simulations in evolving structures toward interspersed bent and straight linkers. Based on the 2 categories of locally stable configurations, we expect that the globally stable state of physiological compact chromatin is a combination of zigzag with straight linker DNAs and solenoid with bent linker DNAs. Furthermore, oligonucleosomes simulated without Mg^{2+} (−LH−Mg and +LH−Mg) did not suffer from convergence problems, possibly because of less compact structures that can be sampled more efficiently with our adopted Monte Carlo methodology. All 4 starting configurations converged to similar equilibrium configurations.

Experimental Procedures. ***Nucleosome array templates.*** We developed a stepwise approach allowing a progressing expansion of repeated DNA sequences. First, we constructed several mononucleosome templates containing a nucleosome core-positioning sequence from the original clone 601 DNA (22) plus linker DNA of differing length (205, 207, 209 bp) to change the nucleosome repeat. The detailed nucleosome DNA sequence of the 207 repeat is described in (23). These mononucleosome templates are inserted into pUC19 vector. New inserts are cut with *Xba*I and *Spe*I and ligated into a vector already containing mononucleosome inserts to give a dinucleosome. This procedure was repeated several times resulting in defined nucleosome 12-mers containing either uniform (207 × 12) or periodically changing (205 - 207 - 209) × 4 nucleosomal repeats as well as 24-mer uniform repeats (207 × 24).

Nucleosome array reconstitution. The oligonucleosome DNA templates were isolated from *Escherichia coli* and reconstituted with chicken erythrocyte histones essentially as described (24) but with addition of competitor DNA (25) derived from pUC19 vector at the template to carrier ratio of 2:1. The reconstituted oligonucleosome core arrays were purified by ultracentrifugation in 5–25% sucrose gradient of sucrose in 10 mM Tris, pH 7.5, 1 mM EDTA, for 8 h at 35,000 rpm in a Beckman SW 41 rotor, dialyzed for 48 h against 10 mM HEPES, pH 7.5, 0.1 mM EDTA, 5 mM NaCl, and finally concentrated to A_{260} ~2.0 using Microsep 30K concentrator (Pall). The purified oligonucleosomes core arrays were characterized by micrococcal nuclease mapping, agarose gel electrophoresis, restriction enzyme protection (see Fig. S1*b*) and electron microscopy (Fig. S2 *a* and *b*) to verify the correct number and positioning of the nucleosome cores. Linker histone H5 was isolated from chicken erythrocytes and reconstituted as described (24) at a ratio of 1 molecule per nucleosome to obtain the regular and variable linker histone-containing arrays (LH-arrays)—see Fig. S1*c*. This ratio of histone H5 to nucleosome is equal to its ratio to DNA in native chicken erythrocyte chromatin (26) and has been shown to induce the maximal compactness of chromatin fibers (27). Histone H5 loading was verified by densitometry of polyacrylamide-SDS electrophoresis in the samples that were taken for EMANIC experiments (Fig. S1 *g* and *h*) as well as after Mg^{2+}-precipitation as described in (25) to show quantitative association of the input H5 with the nucleosome arrays (Fig. S1 *i* and *j*).

Biochemical characterization of the nucleosome arrays. After reconstitution and sucrose gradient purification, the purified core arrays were characterized by digestion with restriction endonuclease *Eco*RI with sites residing in the linker (see scheme on Fig. S1*a*) to show that *Eco*RI sites were exposed in the nucleosome arrays confirming nucleosome positioning over the core but not the linker regions. The 2 types of reconstitutes (uniform and variable) had a similar protection of *Eco*RI sites (Fig. S1*b*) showing that the linker was equally exposed to *Eco*RI in the 2 constructs.

Agarose gel electrophoresis of oligonucleosomes shows that both uniform and variable arrays have an equal mobility in the form of core arrays as well as LH-arrays (Fig. S1*d*, lanes without cross-linking). Furthermore, formaldehyde cross-linking in the decondensed form does not significantly alter the particle electrophoretic mobility (Fig. S1*d*, lanes with cross-linking). The purified core- and LH-arrays were further characterized by micrococcal nuclease (MNase) protection to show that nucleosome cores protect ≈145–150 bp DNA and histone H5 additionally protects ≈170 bp DNA in chromatosomes (Fig. S1*e*). The MNase cutting site positions were determined first by end-labeling of the MNase-digestion products with ^{32}P, digestion with *Sty*I and *Alu*I restriction endonucleases (with sites residing in the core) and high resolution "sequencing" electrophoresis in 6% polyacrylamide-urea (23). High resolution mapping shows that in the 207 × 12 arrays, the nucleosome cores occupy the predicted positions protecting sites 106 and 94 with close to single nucleotide precision (Fig. S1*f*, lanes 6 and 8); these sites correspond to sites 34 and 183 in the mononucleosome (Fig. S1*a*); the dyad axis between the 2 sites (at nucleotide 107 in Fig. S1*a*) corresponds to the one previously mapped by DNase I and hydroxyl radical cleavage (28) for the clone 601 nucleosome positioning sequence. Histone H5 symmetrically protects 11-bp DNA fragments on both sides of the nucleosome core (sites 105 and 117 on Fig. S1*f*, lanes 5 and 7) corresponding to sites 23 and 194 in the mononucleosome (Fig. S1*a*) at positions identical to our previous experiments with linker histone H1 ° (23).

Electron microscopy data collection and analysis. Samples for EMANIC analysis were fixed with 0.1% glutaraldehyde, diluted

10–20 times with 50 mM NaCl, and applied to carbon-coated glow-discharged EM grids. Grids were stained with 0.1% uranyl acetate. Some grids were additionally shadowed with platinum at an angle of 10° using electron gun evaporation. Transmission EM of noncross-linked nucleosome arrays was conducted in dark-field mode as before (23). For each sample, nucleosomal arrays containing 12 distinguishable nucleosome cores were selected to score internucleosome interactions. Internucleosomal interactions were scored as positive if nucleosome-size disks (diameter 110 Å) centered over the nucleosome beads on the EM image contacted each other. Standard deviations and standard error of mean were obtained from at least 2 independently reconstituted samples, each fixed, prepared, and counted in triplicate (≈400 nucleosomes per count). *P* values represent probability associated with a Student's 2-sample unequal variance *t test* with a 2-tailed distribution.

Analytical ultracentrifugation. To monitor nucleosome array folding (secondary chromatin structure), we conducted sedimentation velocity experiments using Beckman Optima XL-A ultracentrifuge (31). Sedimentation velocity analysis was conducted using the continuous c(s) distribution model (32) with SEDFIT software (http://www.analyticalultracentrifugation.com).

1. Beard DA, Schlick T (2001) Computational modeling predicts the structure and dynamics of chromatin fiber. *Structure* 9:105–114.
2. Beard DA, Schlick T (2001) Modeling salt-mediated electrostatics of macromolecules: The discrete surface charge optimization algorithm and its application to the nucleosome. *Biopolymers* 58:106–115.
3. Zhang Q, Beard DA, Schlick T (2003) Constructing irregular surfaces to enclose macromolecular complexes for mesoscale modeling using the discrete surface charge optimization (DISCO) algorithm. *J Comput Chem* 24:2063–2074.
4. Sun J, Zhang Q, Schlick T (2005) Electrostatic mechanism of nucleosomal array folding revealed by computer simulation. *Proc Natl Acad Sci USA* 102:8180–8185.
5. Arya G, Schlick T (2006) Role of histone tails in chromatin folding revealed by a mesoscopic oligonucleosome model. *Proc Natl Acad Sci USA* 103:16236–16241.
6. Arya G, Zhang Q, Schlick T (2006) Flexible histone tails in a new mesoscopic oligonucleosome model. *Biophys J* 91:133–150.
7. Arya G, Schlick T (2007) Efficient global biopolymer sampling with end-transfer configurational bias Monte Carlo. *J Chem Phys* 126:044107.
8. Arya G, Schlick T (2009) A tale of tails: How histone tails mediate chromatin compaction in different salt and linker histone environments. *J Phys Chem A* 113:4045–4059.
9. Luger K, Mader AW, Richmond RK, Sargent DF, Richmond TJ (1997) Crystal structure of the nucleosome core particle at 2.8Å resolution. *Nature* 389:251–260.
10. Davey CA, Sargent DF, Luger K, Maeder AW, Richmond TJ (2002) Solvent mediated interactions in the structure of the nucleosome core particle at 1.9Å resolution. *J Mol Biol* 319:1097–1113.
11. Bednar J, Horowitz RA, Dubochet J, Woodcock CL (1995) Chromatin conformation and salt-induced compaction: Three-dimensional structural information from cryoelectron microscopy. *J Cell Biol* 131:1365–1376.
12. Carruthers LM, Hansen JC (2000) The core histone N termini function independently of linker histonesduring chromatin condensation. *J Biol Chem* 275:37285–37290.
13. van Holde K, Zlatanova J (1996) What determines the folding of the chromatin fiber? *Proc Natl Acad Sci USA* 93:10548–10555.
14. Kepert JF, et al. (2003) Conformation of reconstituted mononucleosomes and effect of linker histone H1 binding studied by scanning force microscopy. *Biophys J* 85:4012–4022.
15. Toth K, Brun N, Langowski J (2006) Chromatin compaction at the mononucleosome level. *Biochemistry* 45:1591–1598.
16. Bharath MM, Chandra NR, Rao MR (2003) Molecular modeling of the chromatosome particle. *Nucleic Acids Res* 31:4264–4274.
17. Bharath MM, Chandra NR, Rao MR (2002) Predictions of an HMG-box fold in the C-terminal domain of histone H1: Insights into its role in DNA condensation. *Proteins* 49:71–81.
18. Sheng S, Czajkowsky DM, Shao Z (2006) Localization of linker histone in chromatosomes by cryo-atomic force microscopy. *Biophys J* 91:L35–L37.
19. Rouzina I, Bloomfield VA (1998) DNA bending by small, mobile multivalent cations. *Biophys J* 74:3152–3164.
20. Baumann CG, Smith SB, Bloomfield VA, Bustamante C (1997) Ionic effects on the elasticity of single DNA molecules. *Proc Natl Acad Sci USA* 94:6185–6190.
21. Richmond TJ, Davey CA (2003) The structure of DNA in the nucleosome core. *Nature* 423:145–150.
22. Lowary PT, Widom J (1998) New DNA sequence rules for high affinity binding to histone octamer and sequence-directed nucleosome positioning. *J Mol Biol* 276:19–42.
23. Nikitina T, et al. (2007) MeCP2-Chromatin interactions include the formation of chromatosome-like structures and are altered in mutations causing Rett syndrome. *J Biol Chem* 282:28237–28245.
24. Springhetti EM, et al. (2003) Role of the M-loop and reactive center loop domains in the folding and bridging of nucleosome arrays by MENT. *J Biol Chem* 278:43384–43393.
25. Huynh VAT, Robinson PJJ, Rhodes D (2005) A method for the in vivo reconstitution of a defined 30 nm chromatin fiber containing stoichiometric amounts of the linker histone. *J Mol Biol* 345:957–968.
26. Bates DL, Thomas JO (1981) Histones H1 and H5: One or two molecules per nucleosome? *Nucleic Acids Res* 9:5883–5894.
27. Robinson PJ, Fairall L, Huynh VA, Rhodes D (2006) EM measurements define the dimensions of the "30-nm" chromatin fiber: Evidence for a compact, interdigitated structure. *Proc Natl Acad Sci USA* 103:6506–6511.
28. Wu C, Travers A (2004) A 'one-pot' assay for the accessibility of DNA in a nucleosome core particle. *Nucleic Acids Res* 32:e122.
29. Schwarz PM, Felthauser A, Fletcher TM, Hansen JC (1996) Reversible oligonucleosome self-association: Dependence on divalent cations and core histone tail domains. *Biochemistry* 35:4009–4015.
30. Woodcock CL, Dimitrov S (2001) Higher order structure of chromatin and chromosomes. *Curr Opin in Gen Dev* 11:130–135.
31. Carruthers LM, Schirf VR, Demeler B, Hansen JC (2000) Sedimentation velocity analysis of macromolecular assemblies. *Methods Enzymol* 321:66–80.
32. Schuck P (2000) Size-distribution analysis of macromoleculars by sedimentation velocity ultracentrifugation and lamm equation modeling. *Biophys J* 78:1606–1619.

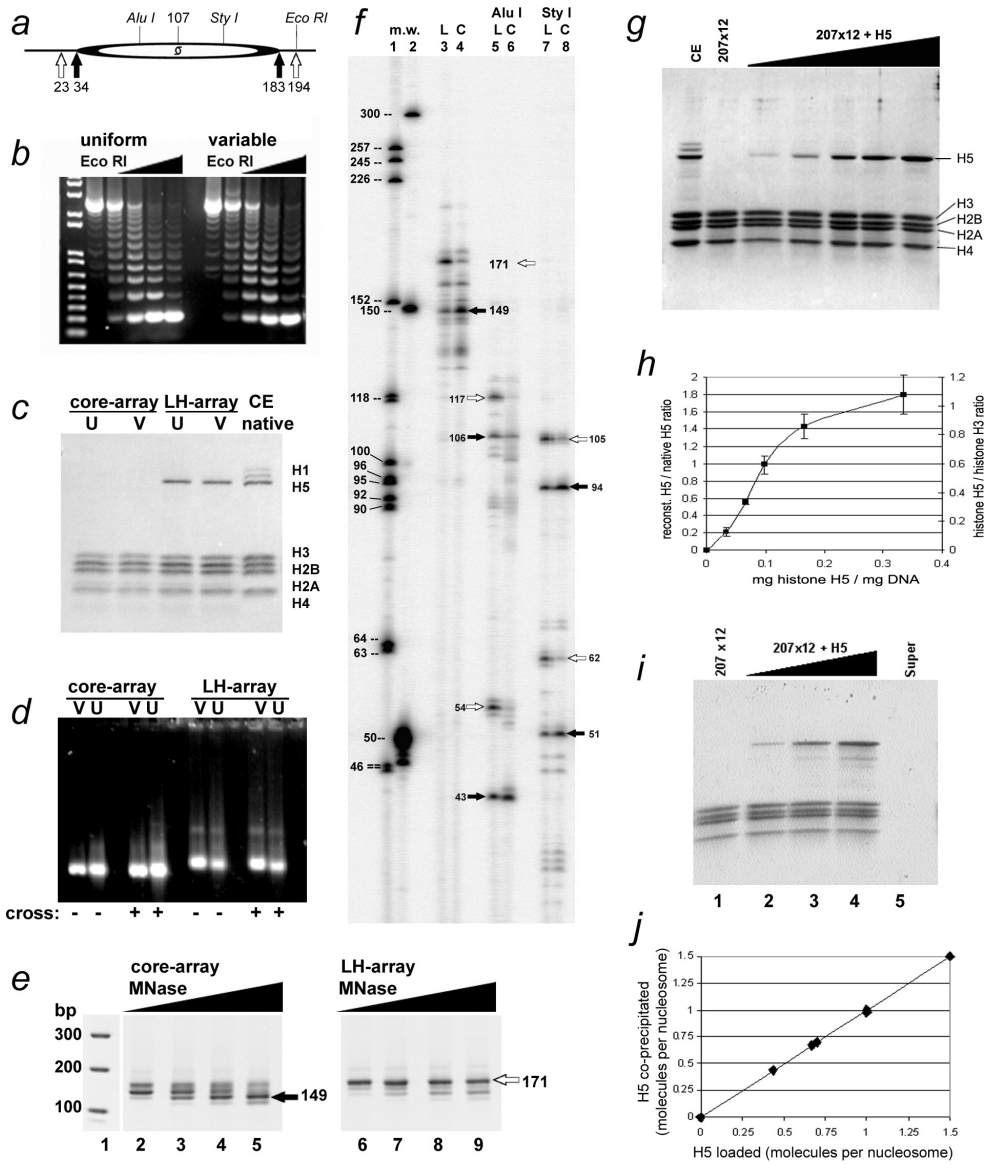

Fig. S1. Characterization of the uniform and the variable nucleosome arrays. (*a*) A scheme of a single nucleosome repeat in the 207 × 12 arrays. The oval represents the nucleosome core particle with dyad indicated. Vertical arrows delineate the nucleosome core (filled arrows) and the chromatosome (open arrows). The positions of restriction enzyme sites used in the nucleosome position mapping (*b* and *f*) are shown by vertical lines. (*b*) Uniform and variable core-arrays were digested with *Eco*RI restriction enzyme, and the DNA was isolated and separated on an agarose gel. (*c*) SDS/PAGE showing the proteins from the uniform (U) 207 × 12 and variable (V) (205 - 207 - 209) × 4 core- and LH-arrays and native chicken chromatin. (*d*) Uniform (U) and variable (V) core- and LH-arrays were separated without deproteinization on a native agarose gel either without (−) or with (+) cross-linking with formaldehyde. (*e*) Discontinuous 12% SDS/PAGE of DNA from uniform core- and LH-arrays digested with MNase. Lane 1 shows a molecular weight marker. (Lanes 2–5) Core arrays digested with MNase for 2.5 (lane 2), 5 (lane 3), 7.5 (lane 4), and 10 (lane 5) min show a resistant band at 149 bp representing the nucleosome core (filled arrow). (Lanes 6–9) LH-arrays digested with MNase for 2.5 (lane 6), 5 (lane 7), 7.5 (lane 8), and 10 (lane 9) min show a resistant band at 171 bp representing the chromatosome (open arrow). (*f*) MNase-digested DNA from the 207 × 12 LH-arrays (L) and core-arrays (C) was purified, end-labeled with ^{32}P, and separated on a ''sequencing'' 6% polyacrylamide-urea gel. Lanes 1 and 2 (m.w.) contain molecular weight calibration markers. Lanes 3 and 4 show DNA from the nucleosome LH-arrays (lane 3) and core arrays (lane 4) MNase-digested for 10 min and labeled with ^{32}P. (Lanes 5–8) ^{32}P-labeled DNA was additionally digested by restriction endonucleases *Alu*I (lanes 5 and 6) and *Sty*I (lanes 7 and 8) to map the positions of MNase cutting sites versus the restriction endopnuclease cutting sites in the nucleosome core. Filled arrows indicate positions of the 149-bp nucleosome ''core'' MNase sites and open arrows indicate the 171-bp ''chromatosome'' sites. (*g*) SDS/PAGE (stained with Coomassie BB R-250) showing the proteins from the native chicken erythrocyte chromatin (CE), uniform core array (207 × 12), and the uniform core array reconstituted with increasing amounts of linker histone H5 (207 × 12 + H5). (*h*) Uniform core arrays were reconstituted with increasing amounts of linker histone H5, the input histone H5 concentration was determined from its sequence-based predicted absorbance of 0.217 for 1 mg/mL H5 protein solution in water at 280 nm (ProtParam at www.expasy.ch). Ratios of reconstituted histone H5 to native histone H5 (left axis) and histone H5 to histone H3 (right axis) were determined by densitometry scanning of 4 PAGE gels like the one shown at *g*. (*i*) SDS/PAGE (stained with Coomassie BB R-250) showing the proteins from the pellets (lanes 1–4) and 1 supernatant (lane 5, corresponding to the pellet in lane 4) of the uniform core array (207 × 12) reconstituted with increasing amounts of linker histone H5 and precipitated by centrifugation at 16,000*g* for 10 min as described (25). (*j*) Ratios of the precipitated histone H5 to the input histone H5 were determined by densitometry scanning of the PAGE gel shown in *i*.

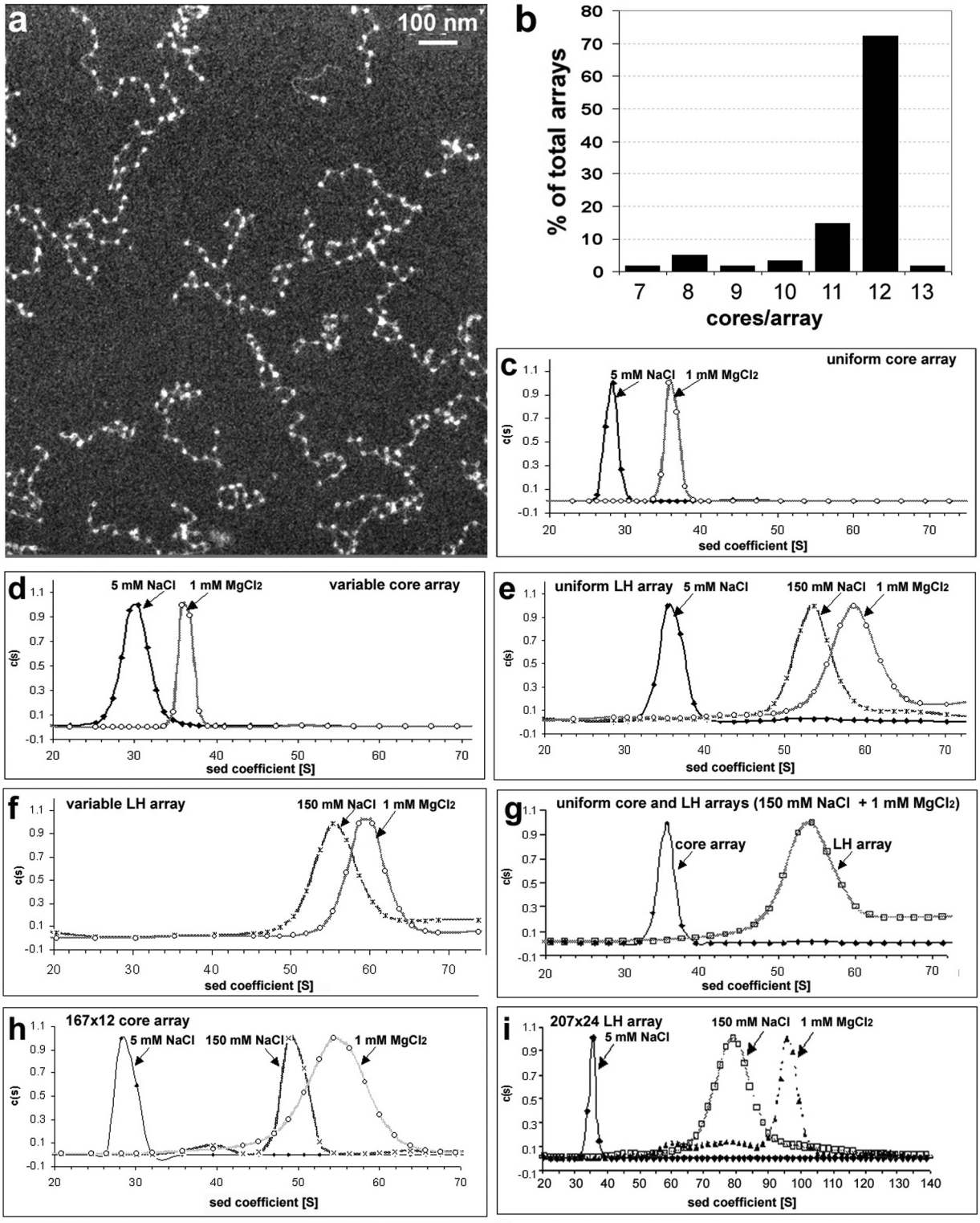

Fig. S2. Structural integrity of the reconstituted nucleosome arrays. (*a*) Electron micrograph (uranyl acetate staining, raw data set) of 207 × 12 core arrays fixed at 5 mM NaCl. (*b*) Histogram showing distribution of nucleosome arrays containing a certain number of nucleosomes per array calculated from several EM fields obtained with the same sample. (*c–i*) Sedimentation coefficient distributions [relative c(s) values] obtained for (*c*) uniform 207 × 12 core arrays at 5 mM NaCl and 1 mM $MgCl_2$, (*d*) variable core arrays at 5 mM NaCl and 1 mM $MgCl_2$, (*e*) uniform 207 × 12 LH-arrays at 5 mM NaCl, 150 mM NaCl, and 1 mM $MgCl_2$, (*f*) variable LH-arrays at 150 mM NaCl and 1 mM $MgCl_2$, (*g*) uniform 207 × 12 core and LH-arrays at 150 mM NaCl plus 1 mM $MgCl_2$, (*h*) uniform 167 × 12 core arrays at 5 mM NaCl, 150 mM NaCl, and 1 mM $MgCl_2$, and (*i*) uniform 207 × 24 LH-arrays at 5 mM NaCl, 150 mM NaCl, and 1 mM $MgCl_2$.

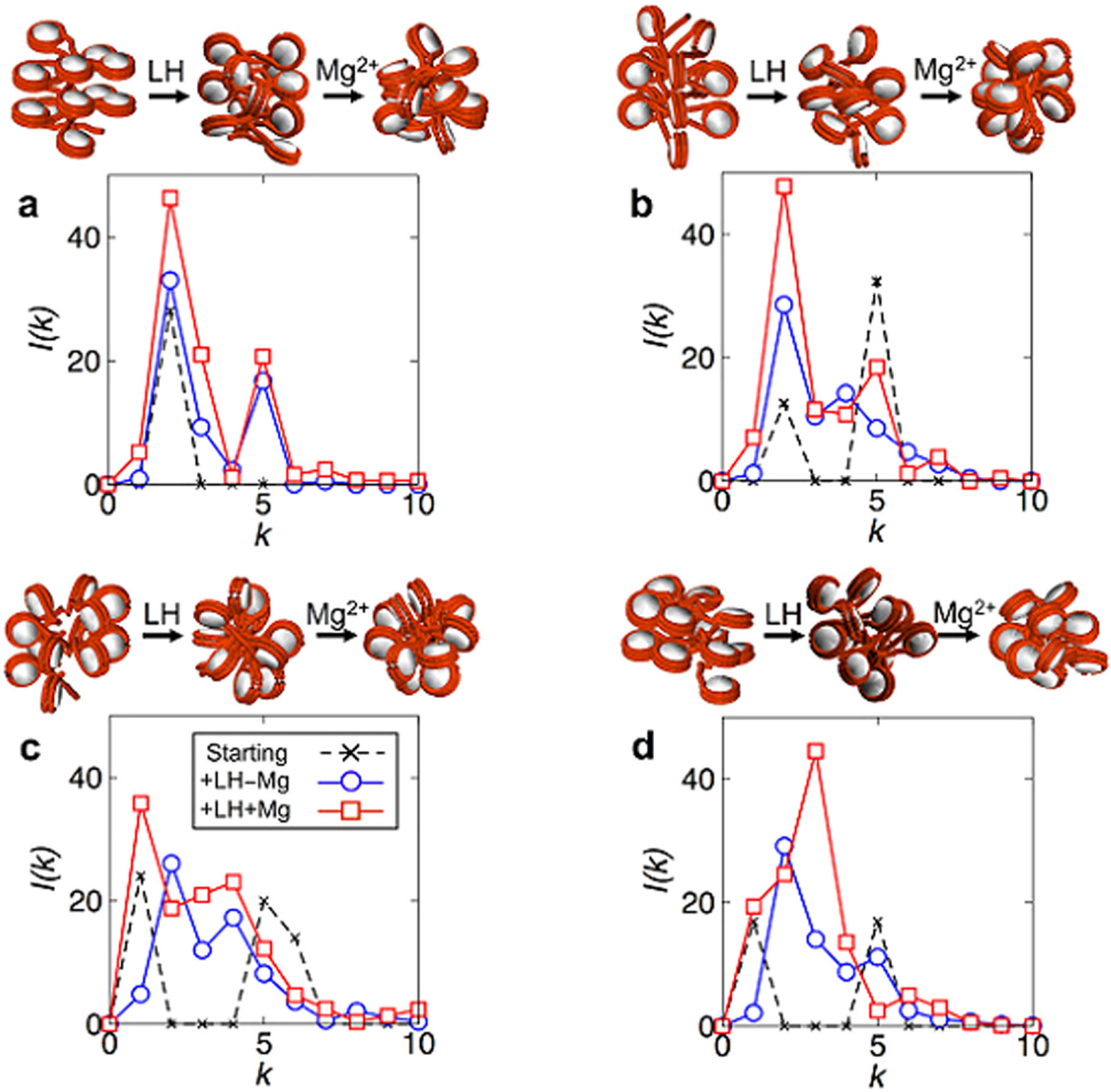

Fig. S3. Monte Carlo simulation of NaCl- and Mg^{2+}-dependent folding of 4 different starting structures. Internucleosomal interaction pattern of LH-inclusive chromatin without Mg^{2+} ions (+LH−Mg) (solid blue lines) and with Mg^{2+} ions (+LH+Mg) (solid red lines) obtained for Monte Carlo simulations started from 4 different oligonucleosome configurations, show initial and final configurations: (*a*) zigzag with parallel nucleosomes, (*b*) zigzag with perpendicular nucleosomes, (*c*) solenoid with perpendicular nucleosomes, and (*d*) solenoid with parallel nucleosomes. Black dashed lines correspond to the internucleosomal pattern of the starting oligonucleosome structure. For the divalent ion simulations, starting configurations *a* and *d* lead to fibers with relatively straight/gently bent DNA, whereas *b* and *c* lead to a small fraction (~18%) of bent linker DNAs. This bending was quantified by measuring the angle between the departing linker DNA in the next nucleosome: It averaged ≈45° without magnesium ions but displayed an additional minor peak ≈100° for the configurational ensemble with magnesium ions (see Fig. S6).

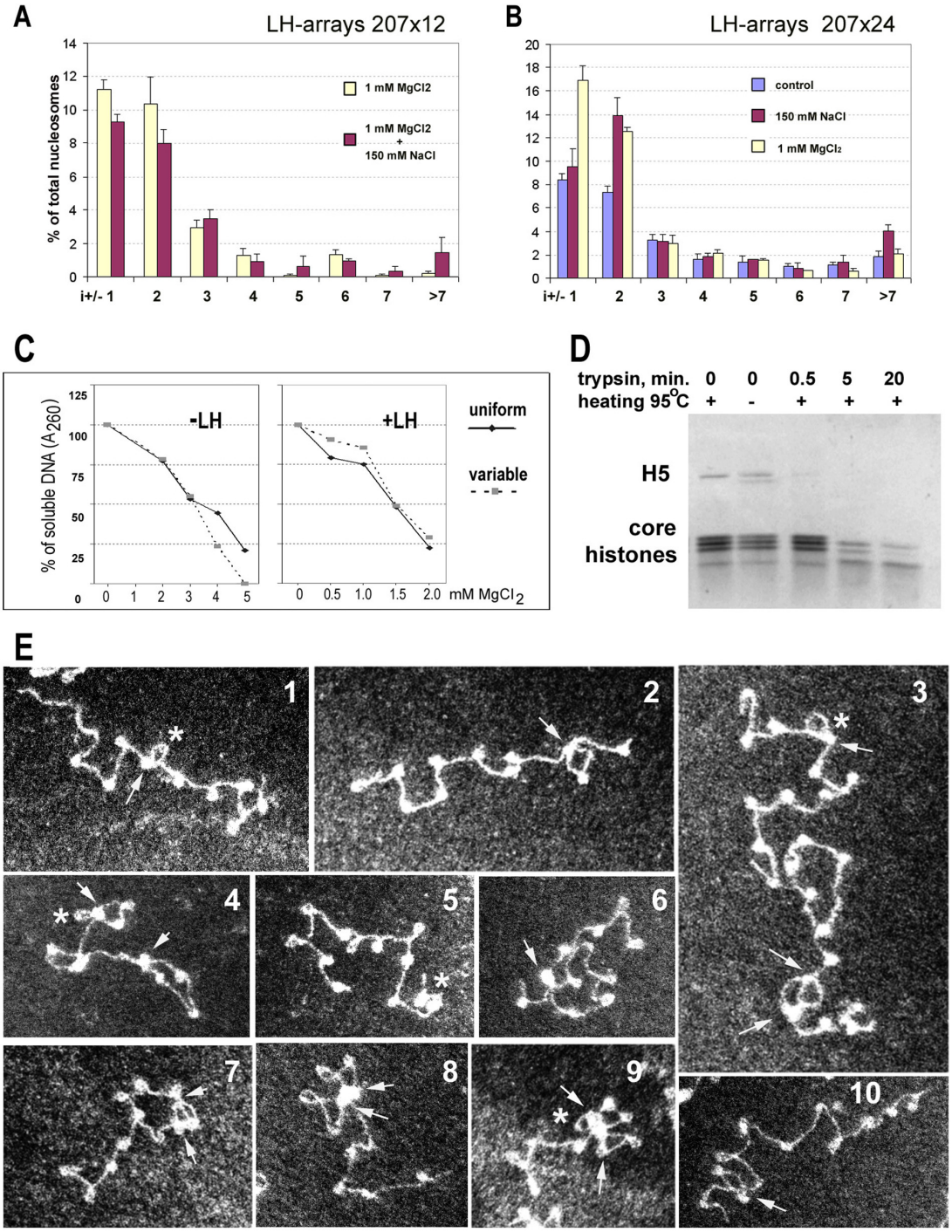

Fig. S4. Probing nucleosome interactions inside condensed chromatin structures. (*A*) Internucleosomal interactions within reconstituted 207 × 12 LH-arrays scored after formaldehyde-cross-linking in the compact form (sedimentation coefficients are shown in Fig. S2*e* and *g*) in the presence of either 1 mM $MgCl_2$ or 1 mM $MgCl_2$ plus 150 mM NaCl. (*B*) Internucleosomal interactions within reconstituted 207 × 24 LH-arrays scored after formaldehyde-cross-linking in the unfolded form at 5 mM Na^+ (control), and in the compact form (sedimentation coefficients are shown in Fig. S2*i*) in the presence of either 150 mM NaCl or 1 mM $MgCl_2$. Histograms show % total nucleosomes involved in interactions between nearest neighbor (i ± 1) and loops (i ± 2 and more). (*C*) Precipitation assays for Mg-dependent oligonucleosome self-association using uniform and variable −LH arrays (left graph) and +LH arrays (right graph) were carried out as described (29). Graphs show percentage of total DNA (A_{260}) remaining soluble after incubation with indicated amount of $MgCl_2$. (*D*) SDS/PAGE of histones from uniform +LH arrays that were cross-linked with formaldehyde at 4 mM $MgCl_2$ and then digested with 1 μg/mL trypsin (T8003; Sigma) at +37 °C for indicated periods of time. Histones were heated for 30 min at +95 °C before electrophoresis to reverse formaldehyde cross-linking. (*E*) EM of uniform +LH+Mg arrays cross-linked with formaldehyde at 4 mM $MgCl_2$ and imaged after trypsin digestion for 5 min (lanes 1–6) or 20 min (lanes 7–10) and unfolding by dialysis against 10 mM Na-borate, pH 9.0, 0.1 mM EDTA to induce chromatin decondensation. Arrows show nucleosome interactions. Asterisks show interacting nearest-neighbor nucleosomes connected by a short DNA loop.

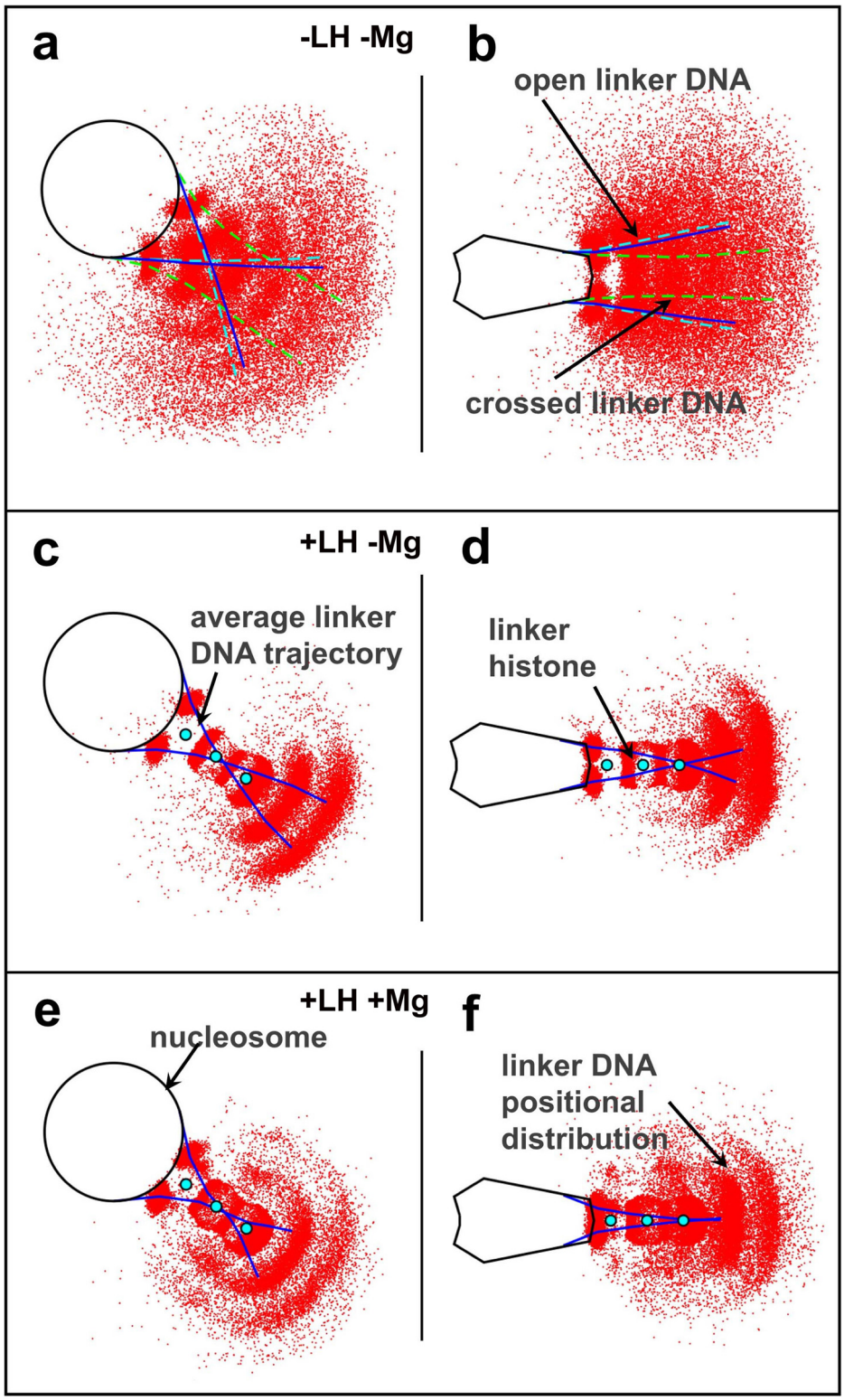

Fig. S5. Effect of linker histone and divalent cation on linker DNA configurations. Linker DNA positional distributions at 0.15 M monovalent salt without LH (*a* and *b*), with LH (*c* and *d*), and with LH and Mg^{2+} (*e* and *f*) are projected onto the nucleosomal (*a*, *c*, *e*) and dyad planes (*b*, *d*, *f*). Red dots represent linker DNA bead positions sampled every 0.1 million steps over the 10-million-step Monte Carlo ensemble. The mean trajectory of the linker DNA beads is shown as solid blue line. The mean trajectories of open and crossed linker DNAs in LH and Mg^{2+} deficient oligonucleosomes (*a* and *b*) are shown as green and cyan dashed lines, respectively. The positions of the 3 LH beads are shown as cyan-shaded circles.

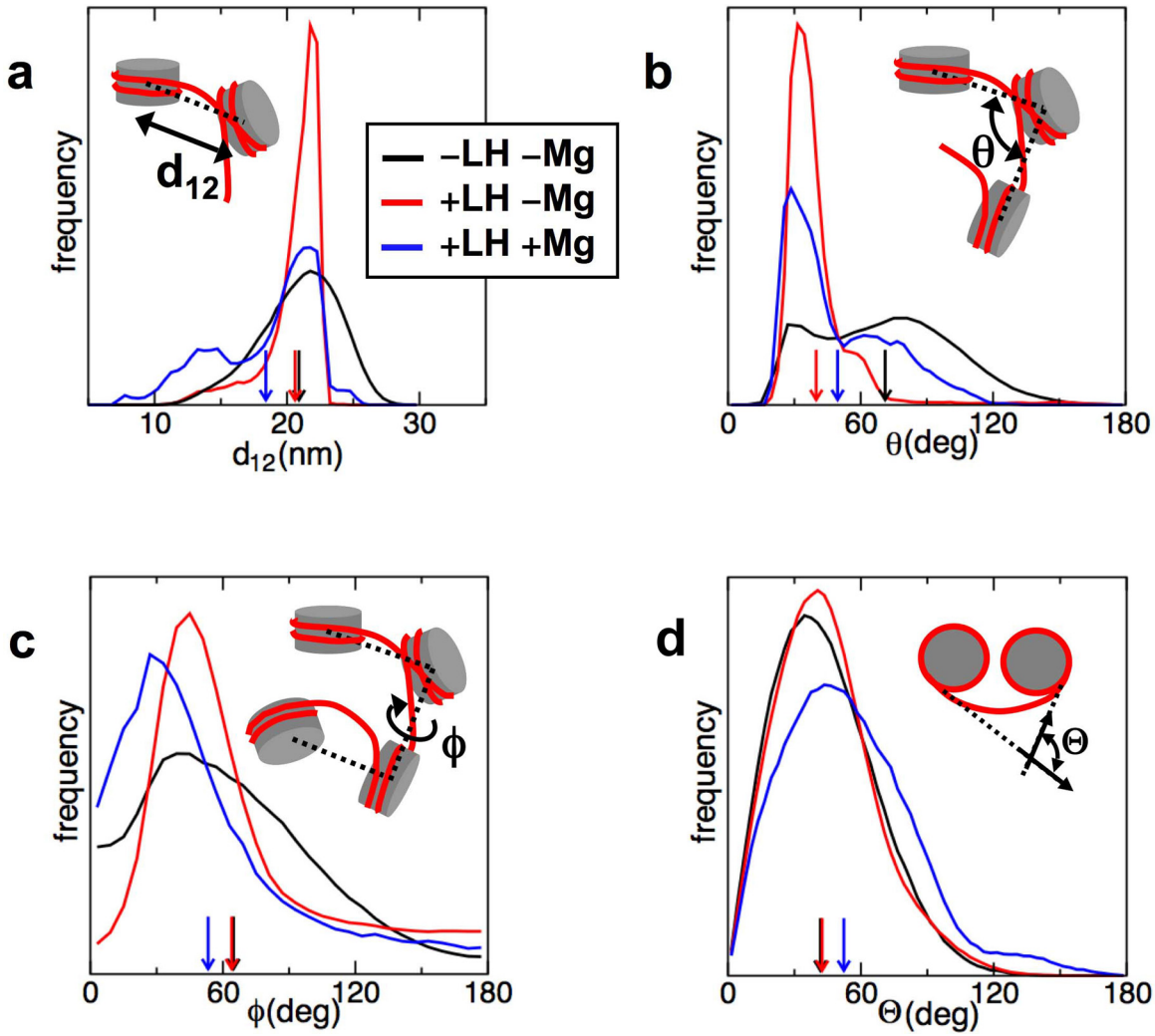

Fig. S6. Geometric features of the chromatin fibers. Frequency histogram of the (*a*) internucleosomal distance, (*b*) triplet angle, (*c*) dihedral angle, and (*d*) linker-DNA bend angle (see text) for 24-unit oligonucleosomes at 0.15 M monovalent salt without LH and Mg^{2+} (black lines), with LH, without Mg^{2+} (red lines), and with LH and Mg^{2+} (blue lines). The mean values of the distributions for the 3 cases are indicated by the black, red, and blue arrows, respectively.

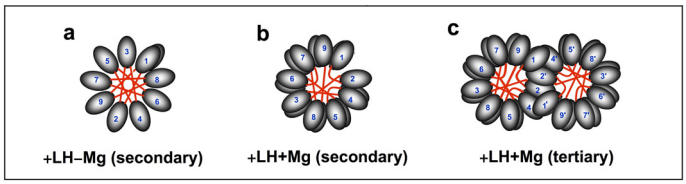

Fig. S7. Schematic models (axial views) considering chromatin higher-order structural levels. (*a*) In the absence of Mg^{2+}, the chromatin fibers fold into a 2-start zigzag and form nonassociated, secondary structures. (*b*) With LH and 1 mM Mg^{2+}, the fibers incorporate partially bent DNA linkers but still maintain the zigzag secondary chromatin structure. (*c*) Increasing the fraction of bent DNA linkers by an elevated concentration of divalent cations (4 mM $MgCl_2$) results in an increased number of open nucleosomal surfaces capable of interacting in *trans* with other nucleosomal fibers and leading to the fiber self-association and formation of the tertiary chromatin higher-order structure (30).